Nature Geoscience

Supporting Information for

# Tracking Transcrustal Magma Ascent Beneath Laguna del Maule, Chile

Authors:

Jim Bradford (1), Sankha Subhra Mahanti (1), Eric Kiser (1), Susan Beck (1),

Martin Fernandez (2), Sol Trad (3,4),

Ryan Porter (5), Sebastian Tauber (5),

Ariane Maharaj (6), Hannah Howe (7),

Gustavo Ortiz (2), Mauro Saez (2,4)

Affiliations:

(1) Department of Geosciences, University of Arizona

(2) Departamento de Geofísica y Astronomía, Universidad Nacional de San Juan

(3) Center for Research on the Geosphere and Biosphere (CIGEOBIO), Universidad Nacional de San Juan

(4) Consejo Nacional de Investigaciones Científicas y Técnicas (CONICET), Universidad Nacional de San Juan

(5) School of Earth Sciences and Environmental Sustainability, Northern Arizona University

(6) Institute of Earth Sciences, University of Lausanne

(7) Department of Physics, University of Alberta

## Introduction

The supporting information here provides additional methodological and model details for the receiver function analysis, focal mechanism catalog, and additional figures supporting the main text.

Contents of this section:

Supplementary Figures S1-S12

Text A1

Table T1

## Supplementary Figures S1-S12

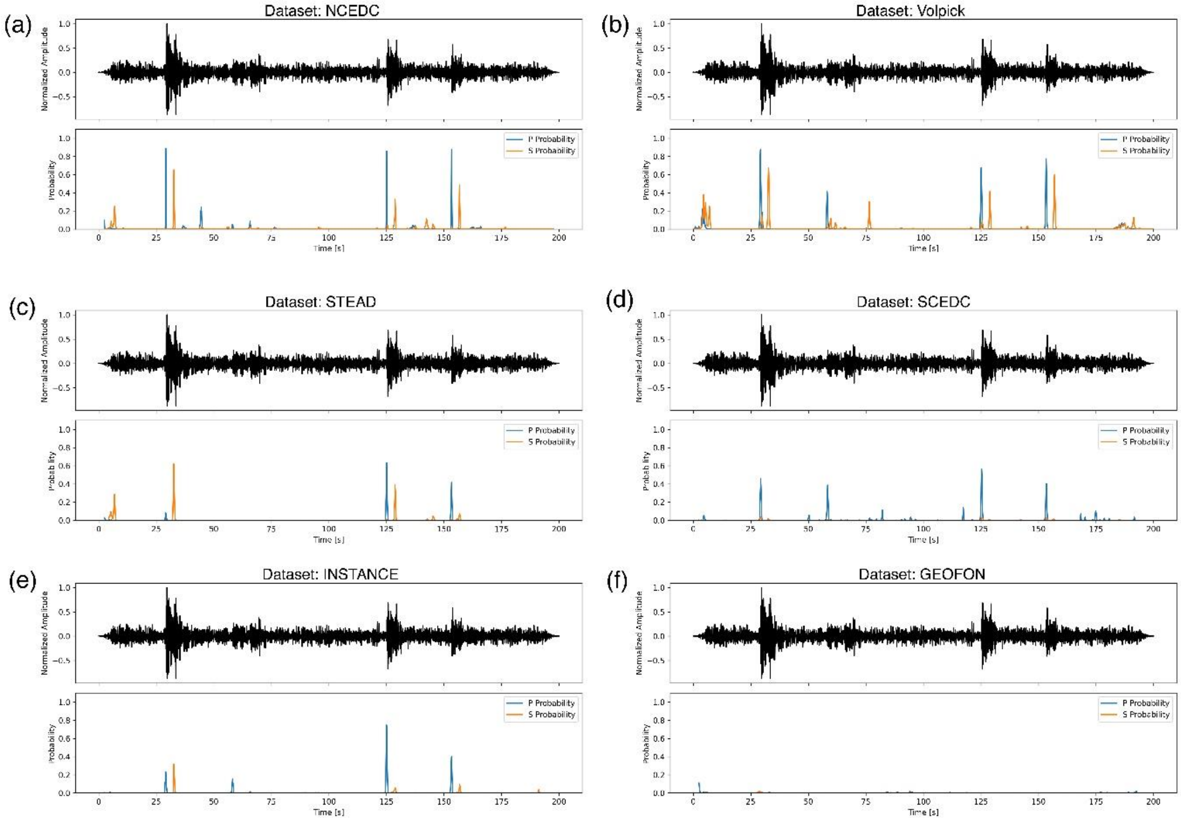

Supplementary Figure S1: Comparison of phase picking performance of PhaseNet with pre-trained models from Seisbench, trained with NCEDC (NCDEC, 2014), Volpick (Zhong & Tan, 2024), STEAD (Mousavi et al., 2019), SCEDC (SCEDC, 2013), INSTANCE (Michelini et al., 2021), and GEOFON (GEOFON Data Centre, 1993) datasets. The original PhaseNet model trained with the NCEDC dataset and Volpick model had the best performance.

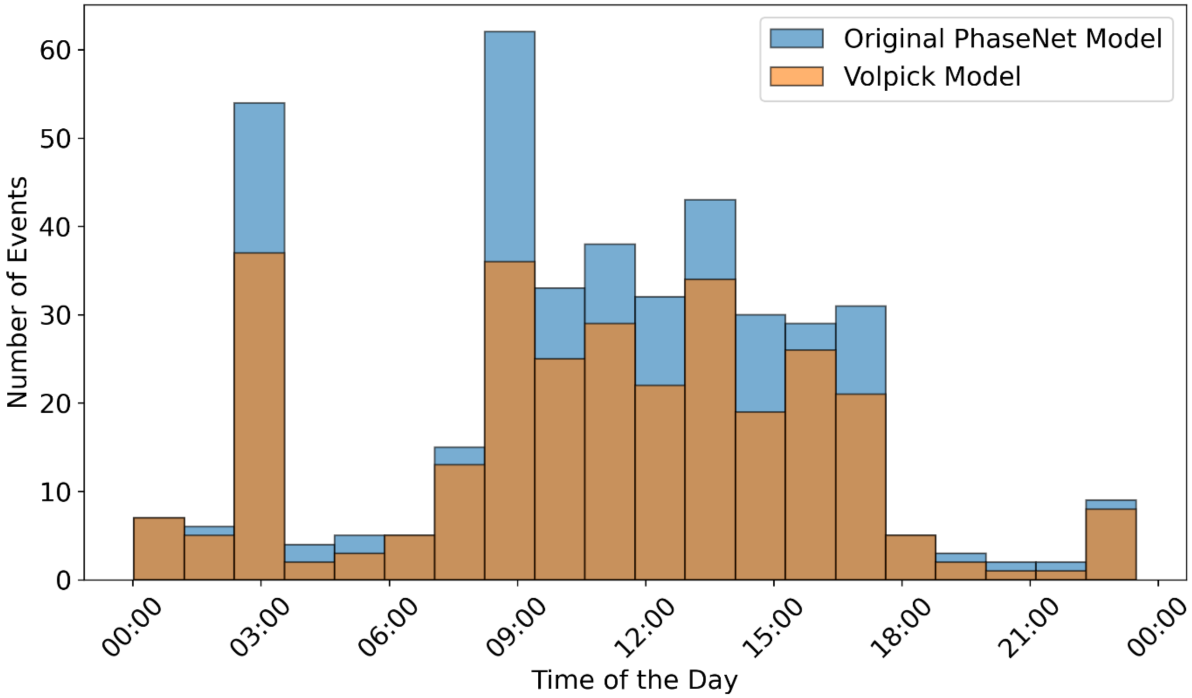

Supplementary Figure S2: Comparison of number of detected events (after initial association) with the original PhaseNet model and Volpick model on February 14, 2018, when the deep VT swarm occurred.

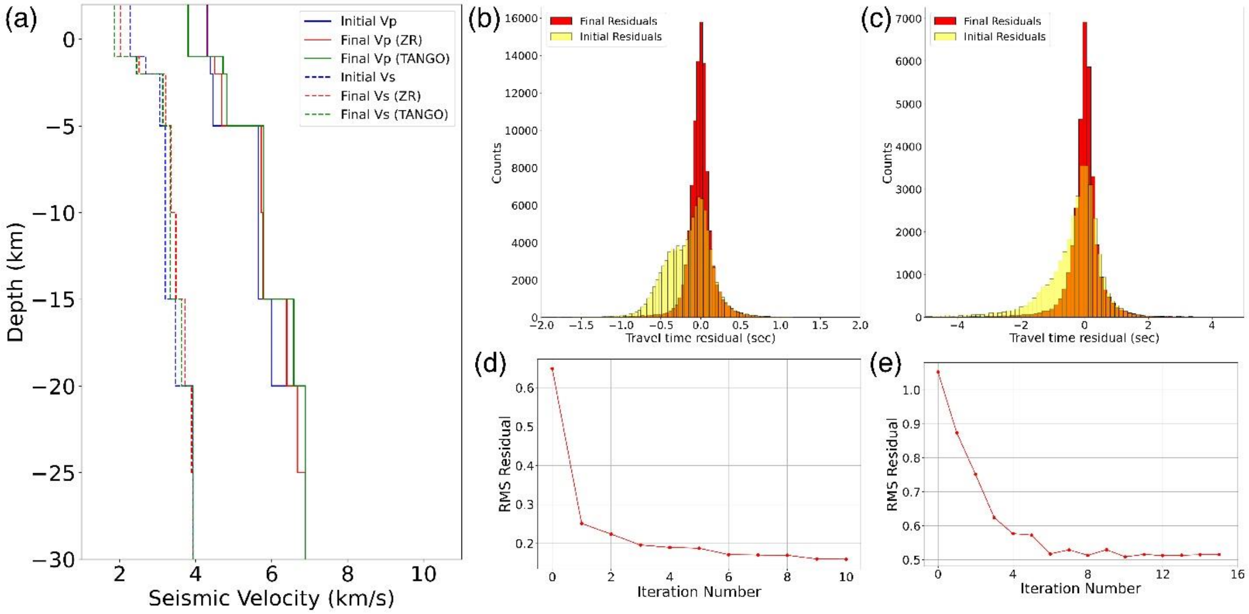

Supplementary Figure S3: (a) Initial Vp and Vs models (blue) from Cardona et al., (2018) and final velocity models after VELEST inversion with catalogs from ZR network (red) and TANGO network (green), (b) Initial and final travel time residuals for VELEST inversion for ZR catalog, (c) Initial and final travel time residuals for VELEST inversion for TANGO catalog, (d) Residual reduction with iterations for ZR catalog, (e) Residual reduction with iterations for TANGO catalog.

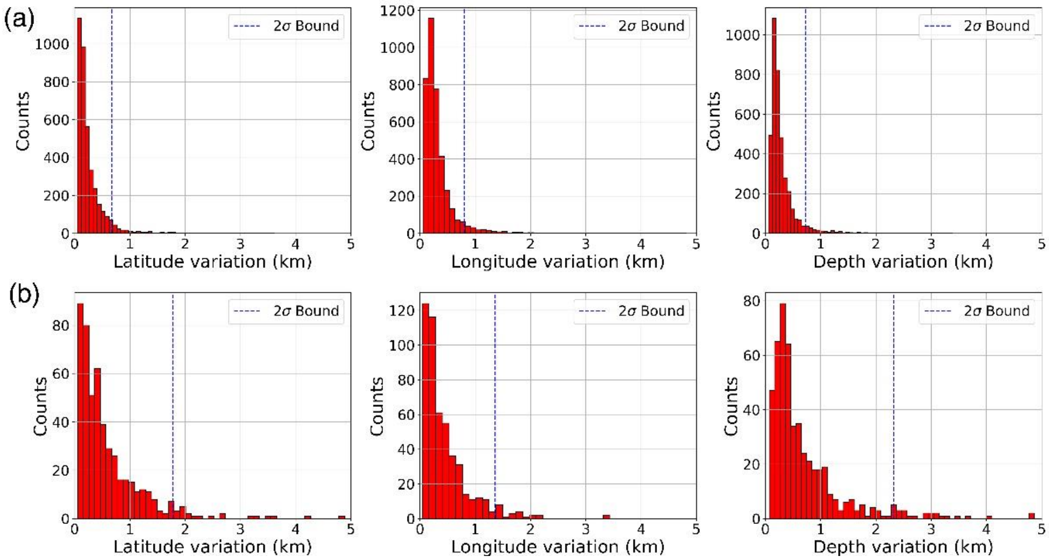

Supplementary Figure S4: Distribution of variations in latitude, longitude, and depth after bootstrap resampling for (a) ZR catalog and (b) TANGO catalog. The blue dashed lines in the plots mark the 2$\sigma$ bounds for these variations.

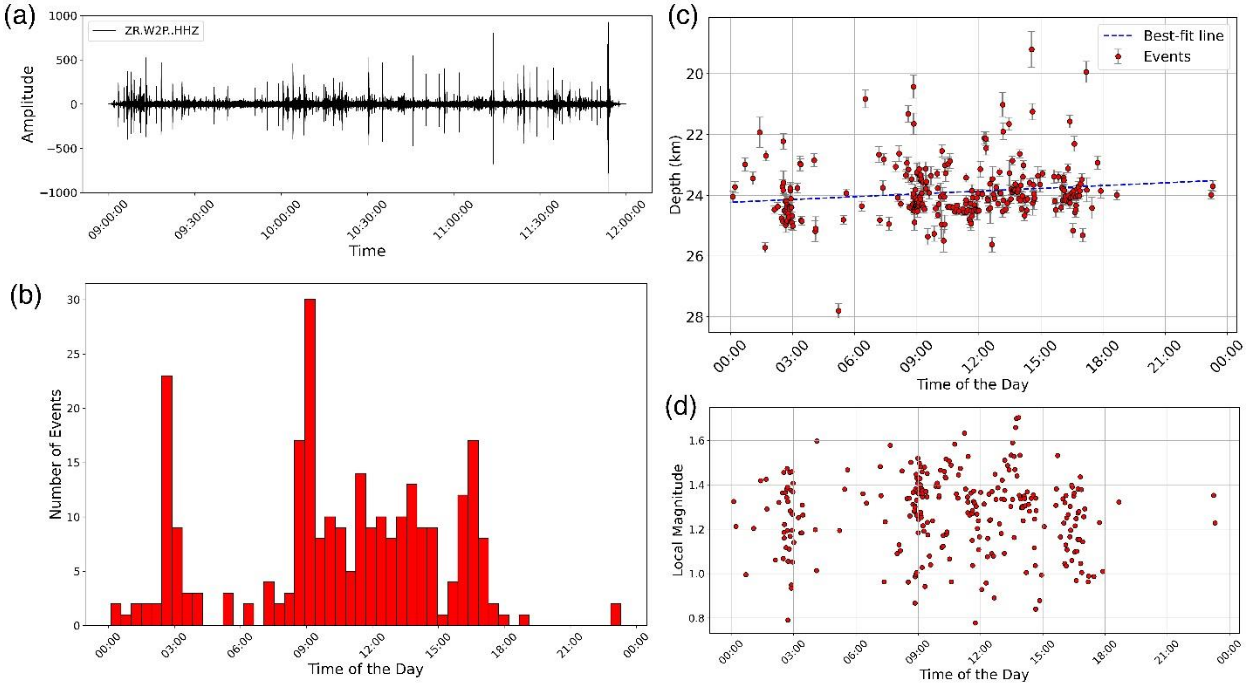

Supplementary Figure S5: (a) Three hours of data on February 14, 2018 at station W2P of ZR network showing the seismic swarm events, (b) Histogram of swarm events for the day, (c) Distribution of depths with time progression where the best fitting line indicates a slight decrease in event depth with time, (d) Distribution of magnitudes with time progression indicating that this is not a mainshock-aftershock sequence.

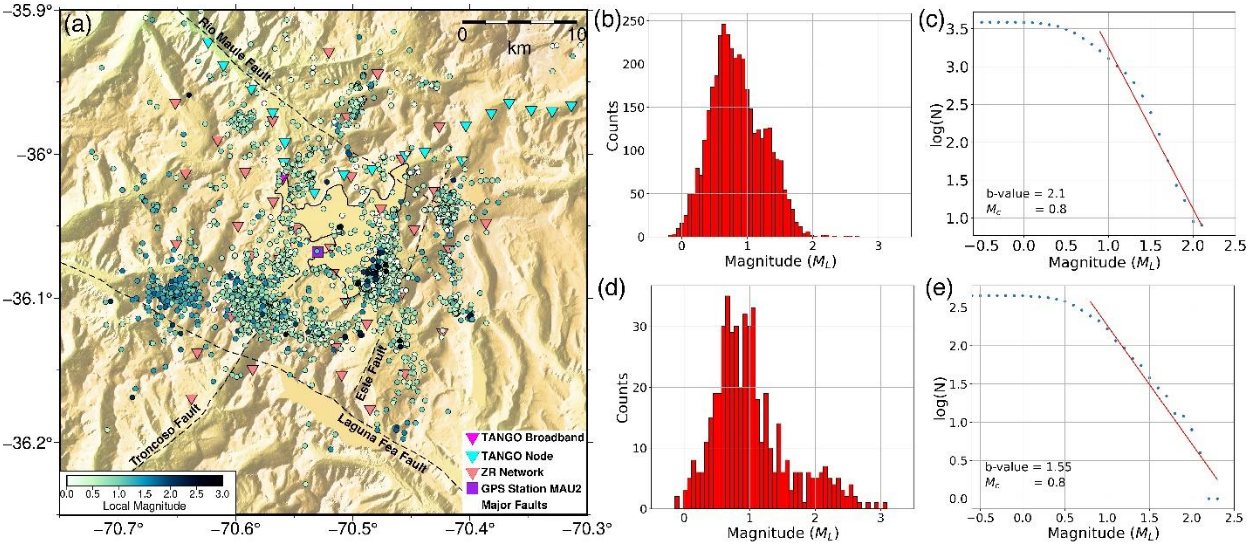

Supplementary Figure S6: (a) Distribution of combined seismicity from ZR and TANGO network color coded by local magnitude. (b) histogram of magnitude distribution and (c) fit to Gutenberg-Richter equation for events in ZR catalog indicating 0.8 as magnitude of completeness ($M_c$) and b-value of 2.1, (d) histogram of magnitude distribution and (e) fit to Gutenberg-Richter equation for events in TANGO catalog indicating 0.8 as magnitude of completeness ($M_c$) and b-value of 1.55. For the TANGO catalog, only the events detected during the time period when the nodal array was active are used for $M_c$ and b-value calculation.

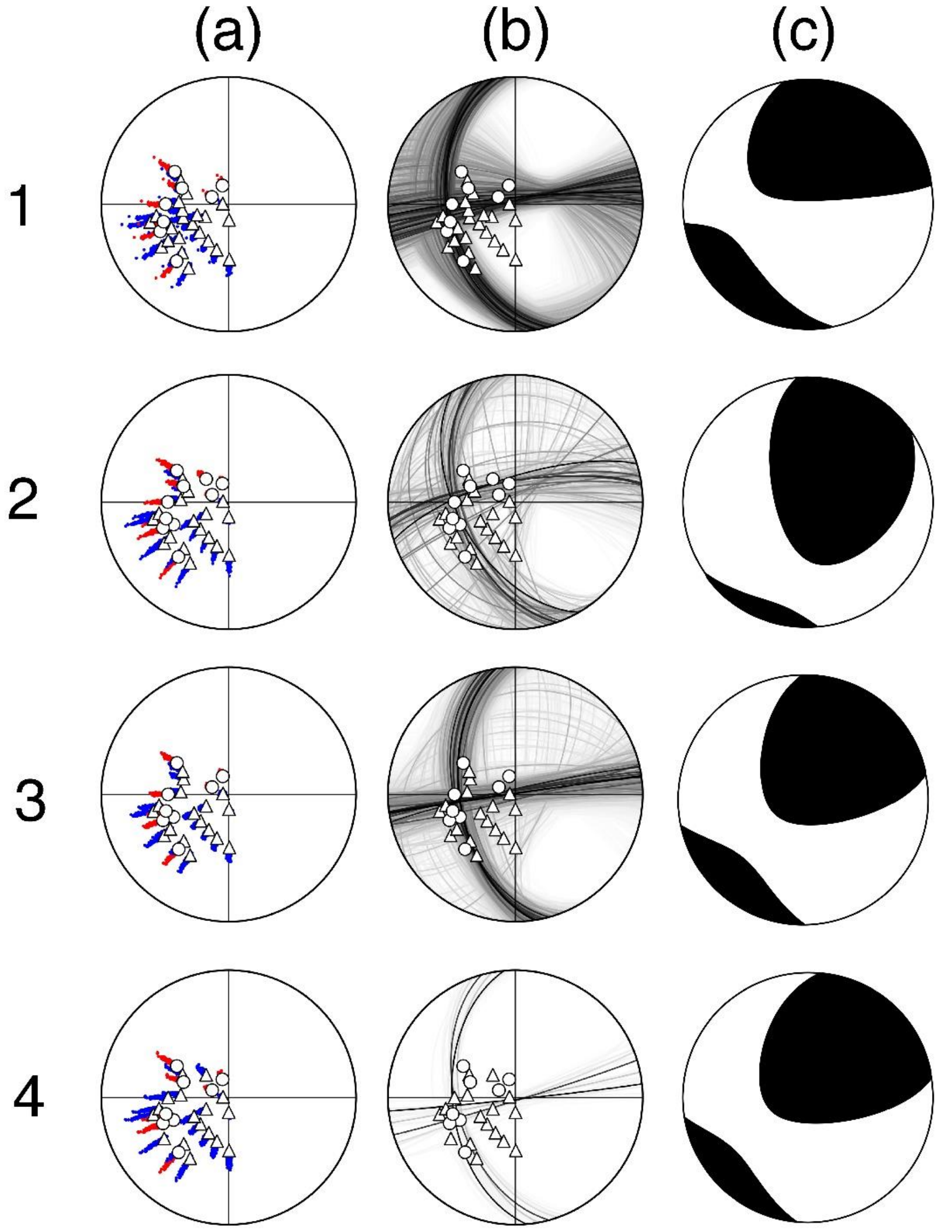

Supplementary Figure S7: Focal mechanism results are shown for 4 events listed in Table S1. For each event, three panels show: (a) Distribution of stations in stereonet projection based upon their azimuth and takeoff angle. Stations with positive polarity observations are marked as circles, and stations with negative polarity observations are marked as triangles. The red and blue dots indicate the variations in positive and negative polarity observations respectively due to variations in azimuth and takeoff angles by considering location and velocity model errors (see methods). (b) Fault plane solutions fitting the polarity observations with darker shades indicating higher probabilities. (c) The full moment tensor solution with highest probability fitting the polarity observations.

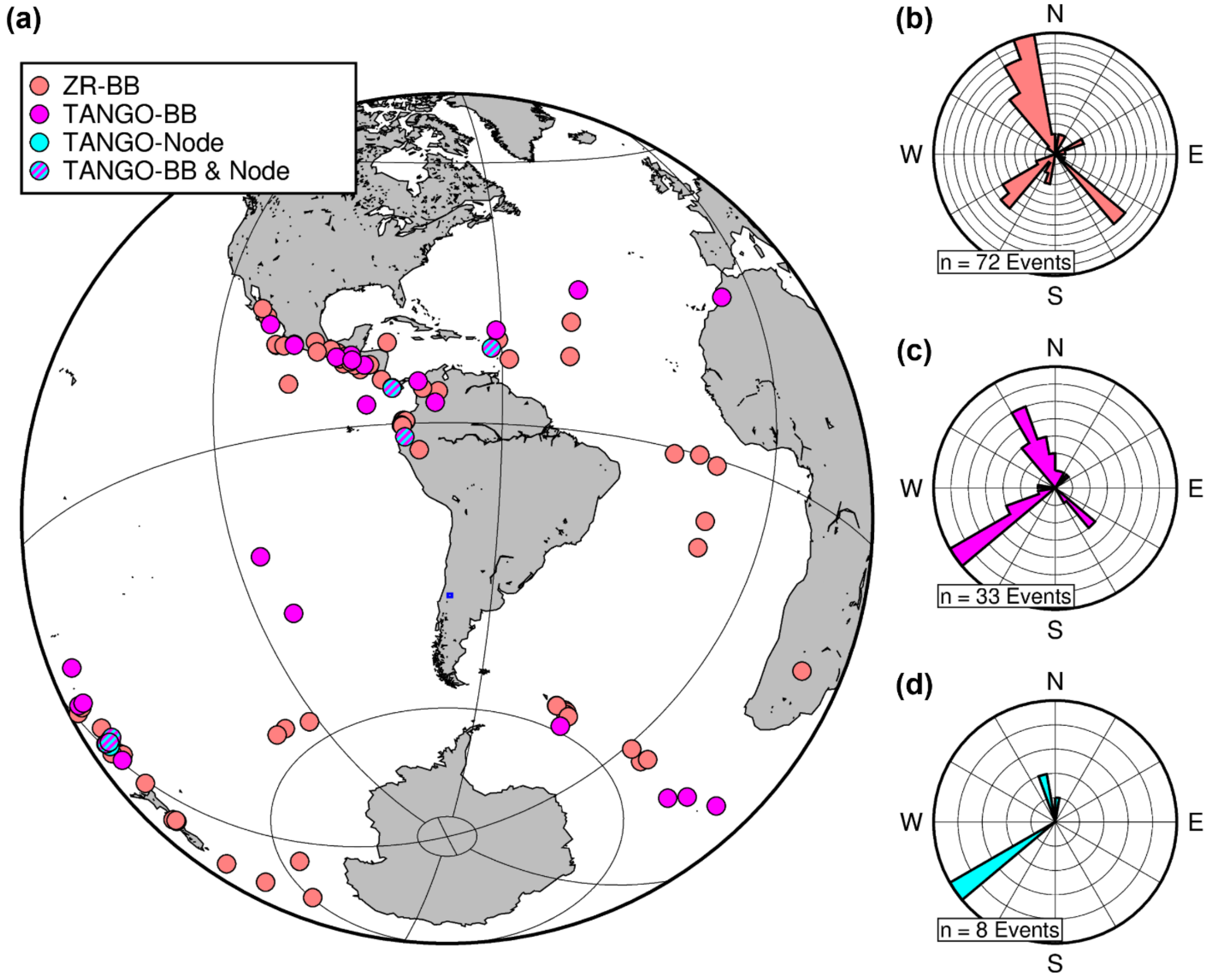

Supplementary Figure S8. (a) Global distribution of teleseismic earthquakes used for receiver function analysis color coded for each network. Rose diagrams are shown for earthquakes recorded on networks (b) Laguna-Maule (ZR), (c) TANGO-Broadband (XM), and (d) TANGO-Node (1X). The events recorded by ZR and XM have a widespread distribution of back-azimuths and ray parameters, enabling a more diverse range for measuring Ps-converting discontinuities around those stations. The 1X network, however, has a more limited event distribution, containing bias for SW-directed rays, which limits the sampling of the crust on the eastern side of the study area.

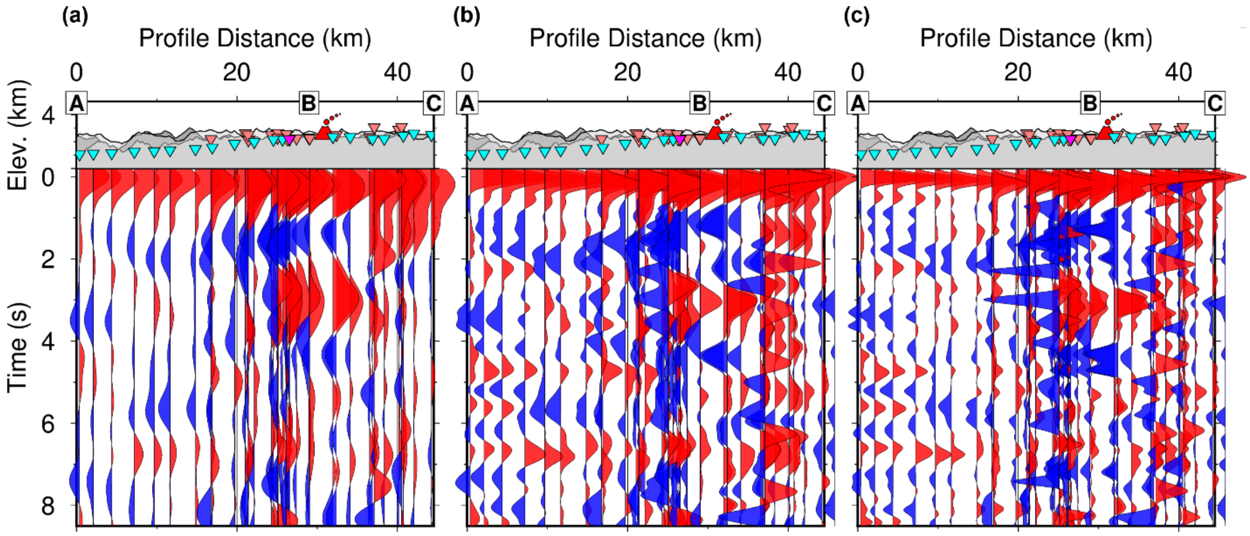

Supplementary Figure S9. Time domain receiver functions along line *ABC in Figure 1*. RFS are calculated with a Gaussian (a) 2.5, (b) 5.0 and (c) 7.5. RFs are projected from 12 km on either side of the *ABC* line. RFs are laterally smoothed by stacking RF within a 4 km radius around each station, the same aperture as the CCP standard deviation weight radius.

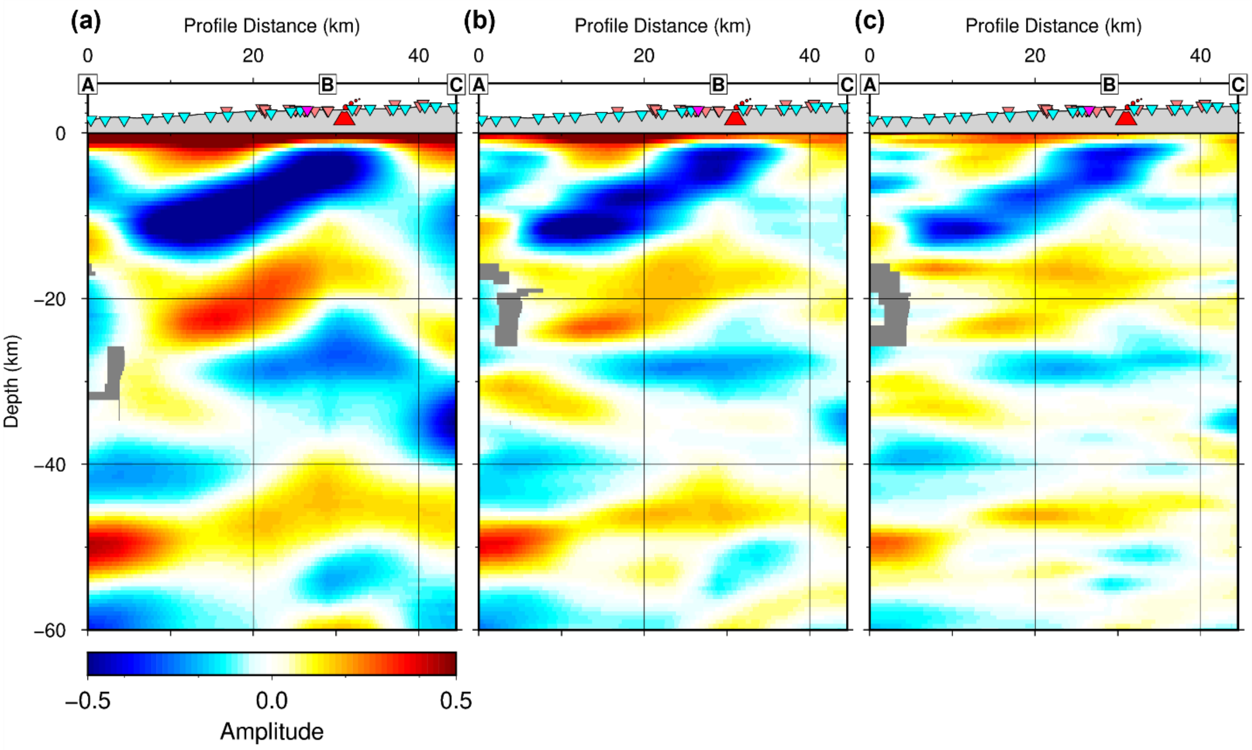

Supplementary Figure S10. CCP Stacking migrated using our preferred 1D VELEST-ZR-mod velocity model using RFs calculated with (a) Gaussian =2.5, 1.2 Hz, (b) Gaussian = 5.0, 2.4 Hz, (c) Gaussian = 7.5, 3.7 Hz. We use a Gaussian of 7.5 in this study.

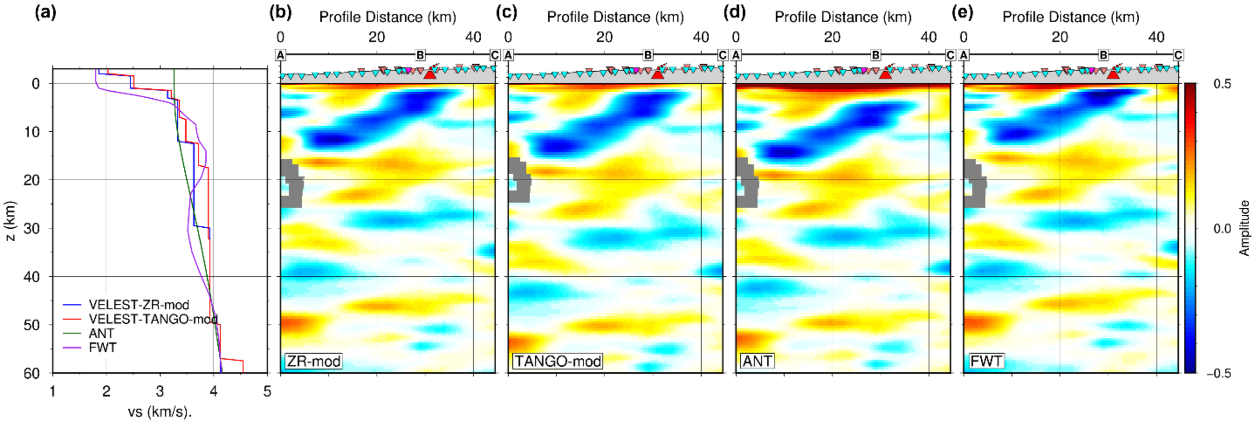

Supplementary Figure S11. Comparison of CCP images migrated with 4 different velocity models using Gaussian=7.5 RFs (3.7 Hz). (a) Plots of 1D S-wave velocity models tested in CCP imaging. (b) CCP image migrated using our preferred model (ZR-mod), modified from the VELEST inversion output with hypocenters using only the ZR network data, (b) CCP image migrated with the modified VELEST output using only the TANGO network (XM & 1X) data, (c) CCP image using the Ambient Noise Tomography velocity model (ANT) by Ward et al., (2013), (d) CCP image using the Ambient Noise Tomography velocity model (FWT) by Liu and Gao (2022).The VELEST models, ZR-mod and TANGO-mod models represent the two extremes of slow and fast shear wave models that have the effect of respectively raising and lowering CCP discontinuities in depth.

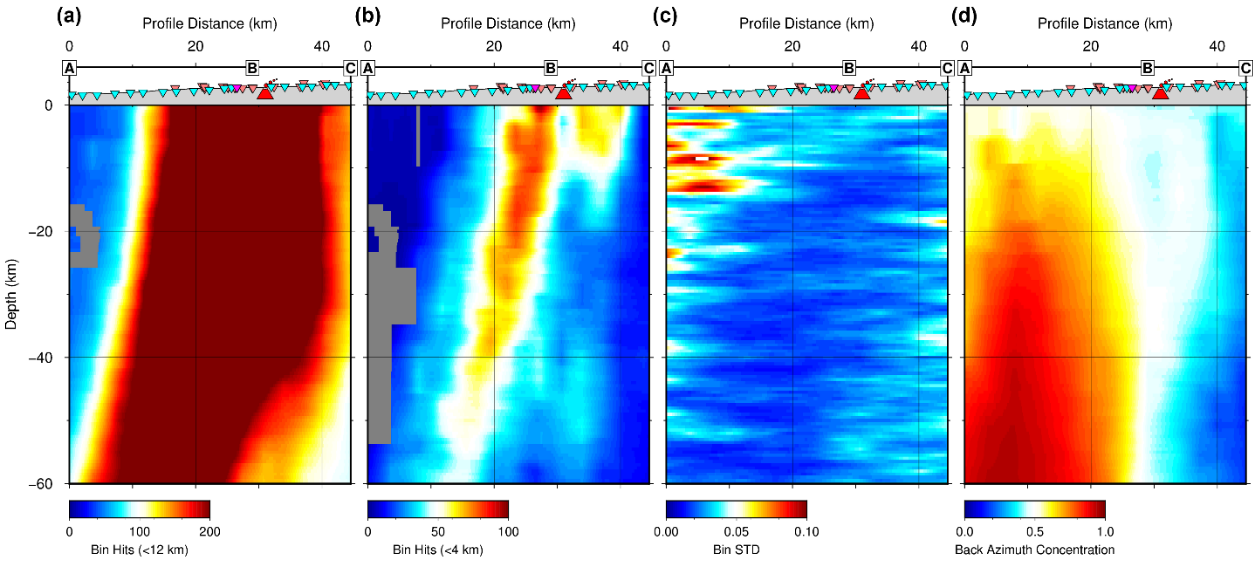

Supplementary Figure S12. Bin statistics from the CCP migration with 3.7 Hz RFs using the 1D VELEST-ZR-mod model. (a) Bin hits within each 12 km bin radius. (b) Bin hits within a 4 km standard deviation radius used in distance-weighted averaging of RF amplitudes. (c) Bin standard deviation of bootstrap resampled RF amplitudes. (d) back-azimuth concentration of bin piercing points, values close to 1 are more concentrated and biased towards a particular back-azimuth whereas values near 0 signify a more even spread of bin piercing points back-azimuths.

| ID | Origin Time | Latitude | Longitude | Depth | Magnitude | Strike | Dip | Rake |
|---|---|---|---|---|---|---|---|---|
| 1 | 2018-02-14T13:33:22.65 | 36.0957 | 70.6503 | 23.74 | 1.669 | 265 | 86 | -135 |
| 2 | 2018-02-14T13:41:46.59 | 36.0955 | 70.6505 | 23.73 | 1.708 | 253 | 74 | -141 |
| 3 | 2018-02-14T13:44:13.03 | -36.0955 | 70.6504 | 23.76 | 1.727 | 261 | 89 | -144 |
| 4 | 2018-02-14T13:50:37.13 | 36.0956 | 70.6505 | 23.78 | 1.746 | 175 | 49 | 2 |

Table T1: List of the four deep events where we calculate focal mechanisms. The strike, dip, and rake are associated with the best-fitting double-couple mechanism.

## A1. Receiver Function Methodology

*Processing Workflow*

Seismic networks contributing to our analysis are XM (Beck et al., 2022a), 1X (Beck et al., 2022b), ZR (Thurber, 2015), and a single station from the YC network (Beck et al., 2000).

The 1X network is made up of 3-component nodal seismometers with a 5 Hz corner frequency. The network includes Smart Solo 3C sensors in Chile and Fairfield Zland 3C sensors in Argentina. The Fairfield sensors (Network 1X, stations 91-240) by default use the industry-standard z-positive direction down and require an additional step of flipping their Z-component traces to conform to the scientific community standard with z-positive up. The XM network consists of broadband sensors.

The complete workflow from data download to CCP computation is wrapped in a sequential series of python scripts. A summary of the workflow is as follows:

1. Download teleseismic data from the IRISDMC at EarthScope (Zawacki et al., 2023) as event-station pairs.
2. Using processed data with the instrument response removed and filtered between 0.1-2.0 Hz, we visually assess the P-wave moveout on the vertical component in a record section for input data quality, and make a list of the passing events with identifiable P-waves across the recording stations.
3. From the list of passing teleseismic events, calculate the signal-to-noise ratio (SNR) for each vertical and horizontal component of event-station pairs with the instrument response removed and filtered between 0.1-8.0 Hz. We construct a list of good data where the event-station pairs have an identifiable P-wave and SNR >2.
4. From the list of quality-controlled event-station pairs, using the raw data we remove the instrument response from all waveforms using a trapezoidal filter with corners of 0.01, 0.1, 8.0, 10.0 Hz. We interpolate data to a sampling rate of 50 samples per second, remove mean and trend, apply Hanning taper, bandpass filter between 0.1-8.0 Hz with two poles and four zeros using SAC (Goldstein & Snoke, 2005). Rotate data to ZRT reference frame. The processed data is saved to be used in the following RF calculation.
5. Calculate receiver functions with iterative time domain (ITD) method (Ligorría & Ammon, 1999).
6. Visually inspect RFs for quality control and eliminate any RF with: (1) A negative first-peak polarity at t=0. This implies a reversal of polarities of the vertical or radial component input data. (2) Long period overprint signal or high amplitude ringing (higher amplitude than the initial P-wave pulse) that may indicate a problem with the input data.
7. Compute common conversion point imaging images using high quality normalized RFs and appropriate seismic velocity model.

### *Data Quality Control*

The downloaded collection of P-waveforms from teleseismic sources contains a mix of data quality. To ensure that clean waveforms with minimal noise were processed into RFs, we implemented a series of quality control steps to remove bad traces. For each quality control step (QC), we maintain a list of passing files that refer back to their originally downloaded raw data file. Among the processing steps, instrument response removal is critical for RF calculation using nodal sensors. The removal of instrument responses is not required for broadband seismometers, as RF deconvolution makes it redundant, but it does help recover a broader frequency band in short period and nodal seismometers (Wölbern et al., 2009; Ward & Lin, 2017). For methodological consistency, the instrument responses were removed regardless of bandwidth type. From the raw data of each passing trace at every pre-RF calculation QC step, we removed the instrument response from all waveforms using the archived instrument response metadata. Instrument response removal parameters include a trapezoidal filter with corners of 0.01, 0.1, 8.0, 10.0 Hz. Data was kept in its original velocity format.

The collection of vertical-component P-waveforms for each teleseismic event was required to have an observable moveout across the network within an event record section. From the raw data, each waveform was cut 30 seconds before and 120 seconds after the IASPEI91 predicted P-wave arrival time, had their instrument responses removed, then were filtered between 0.1 and 2.0 Hz using a Butterworth bandpass filter. If most stations within the record section had a consistent P-wave recording, then the event was accepted for further quality control and stored in a list of quality-controlled events.

Next, the root-mean-square SNR of each vertical and ZRT-rotated radial waveforms that passed record section quality control were calculated using the data 60 seconds before and 60 seconds after the IASPEI91 predicted arrival time (Kennet, 1991). Files that had 2:1 SNR and greater on both components were saved into a list of good data to be used in RF calculation.

### *Receiver Function Calculation*

Radial P-receiver functions are calculated from the deconvolution of the vertical from radial components of a seismogram cut around a teleseismic earthquake P-wave (Burdick & Langston, 1977; Langston, 1979). The RF method isolates P-to-S converted phases (Ps) generated at seismic discontinuities beneath a seismic station. At significant discontinuities in seismic impedance contrast (velocity and density), the transmission of the direct P-wave, energy is partitioned into a P-wave and a vertical shear wave component (Ps phase). The RF method identifies Ps converted phases within the P-wave coda that are recorded on the Radial RF. We use an iterative time domain method (ITD) to calculate the RFs (Ligorría & Ammon, 1999).

ITD solves for an estimated receiver function by iteratively introducing spike delta functions onto a time series that is convolved with the vertical component seismogram to form a predicted radial seismogram waveform. The iterative process continues up until a defined limit (400 iterations) or the predicted radial seismogram has enough similarity to the measured radial waveform within a specified threshold of 70%. The final ITD step is applying a low-pass gaussian filter to smooth the "spike-train". The filter is defined using a Gaussian width parameter *(G),* with a higher Gaussian parameter resulting in a higher frequency RF. We calculate RFs using Gaussians with widths of 2.5, 5.0, and 7.5, which correspond to low pass frequencies of 1.2, 2.4, and 3.7 Hz respectively (Fig. S12). We use a Gaussian width of 7.5 for our interpretation in this study.

### *Common Conversion Point Imaging (CCP)*

The principal purpose of CCP stacking is to migrate the RFs from the time domain to depth. The CCP method has the added benefit of improving the signal to noise ratio of data and correcting for moveout and back-azimuthal differences (Deuker & Sheehan, 1997; Sheehan et al., 2000). When an appropriate velocity model is applied, the RF amplitudes at common subsurface bins are enhanced. The CCP method applied in this study is based on generalized ray theory and simple ray tracing. We assume that conversions occur along laterally continuous and horizontal boundaries, not typically considering the effects of diffraction, dipping interfaces, and scattering around laterally discontinuous features (Sheehan et al., 2000; Rondenay, 2009). The small station spacing of 2-3 km (which enables smaller CCP binning) improves the overall coherency of the final CCP image.

### *Velocity Model Selection*

We utilize a modified version of the output 1D velocity model from the VELEST hypocenter relocation of the earthquakes using the data from the ZR network to migrate the RFs for the CCP images (Figure S10(a)). We modify the ZR VELEST model to have a crustal thickness of 55 km. We compare the CCP images using this velocity model and another VELEST output model (from the TANGO VELEST model also modified with a crustal thickness of 55 km), and two publicly available 3D shear-wave models for this region from the IRIS DMC Earth Models depository (IRIS DMC, 2011) (Figure S10).

No crustal model includes an upper and lower crust LVZ that we identify from our RF observations, which impacts the accuracy of migrated discontinuity depths. LVZs increase the delay time between direct P and Ps converted phases. Hence, a model that is on average-overall faster tends to "push down" discontinuities to greater depth when migrating. Figure S10 shows a comparison of CCP images migrated with four different velocity models. The 1D VELEST output model using the TANGO node and broadband data contains the highest overall shear wave velocities below 5 km depth. This tends towards a thicker crust after migration, ~51 km under the LdM complex. The VELEST output using the ZR network data is marginally slower (~49 km *bsl* Moho) and likely more representative of our area of interest directly beneath the volcanic complex. The initial VELEST model has a 35 km thick crust (crustal thickness of the IASPEI starting model), hence, we modified the crust by expanding the crustal velocities to 55 km depth with mantle values below 55 km. This produces the overall bulk-slowest model, which migrates the Ps conversions to shallower depths (~46 km *bsl* Moho under LdM). Migrating with the Ambient Noise Tomography model from Liu and Gao (2022) produced similar crustal thickness to the modified VELEST-ZR model. All other models resulted in Moho depths between these values (Supplementary Figure S10).

The velocities in the upper 5 km of the crust are not well resolved in the models. Due to significant differences in velocity within the upper 5 km. The resultant differences in the CCP images between these velocity models is that when faster velocities are applied to the upper 5 km, the migration pushes the LdM top discontinuity deeper. Slower models bring the top of the LVZ to shallower depths. We prefer to use the modified VELEST-ZR model so that we can compare the seismicity and RF processes with the same seismic velocity model.

## References

Beck, S., Porter, R., Roecker, S., & Kiser, E. (2022a). *TANGO, Collaborative Research: TransANdean Great Orogeny, Broadbands/Argentina deployment* (EarthScope Data Center (IRISDMC). https://www.fdsn.org/networks/detail/XM_2022/

Beck, S., Porter, R., Roecker, S., & Kiser, E. (2022b). *TANGO, Collaborative Research: TransANdean Great Orogeny, Nodes/Chile deployment* (EarthScope Data Center (IRISDMC). https://www.fdsn.org/networks/detail/XN_2022/

Beck, S., Wallace, T., & Zandt, G. (2000). *Slab Geometry in the Southern Andes* (https://doi.org/https://doi.org/10.7914/sn/yc_2000

Burdick, L. J., & Langston, C. A. (1977). Modeling crustal structure through the use of converted phases in teleseismic body-wave forms. *Bulletin of the Seismological Society of America*, *67*(3), 677-691. https://doi.org/10.1785/BSSA0670030677

Deuker, K. G., & Sheehan, A. F. (1997). Mantle discontinuity structure from midpoint stacks of coverted P to S waves across the Yellowstone hotspot track. *Journal of Geophysical Research*, *102*, 8313-8327.

GEOFON Data Centre. (1993). *GEOFON Seismic Network* (GFZ Data Services. https://doi.org/doi:10.14470/TR560404

Goldstein, P., & Snoke, A. (2005). SAC availability for the IRIS community. *Incorporated Research Institutions for Seismology Newsletter*, *7*(UCRL-JRNL-211140).

IRIS DMC. (2011). Data Services Products: EMC, A repository of Earth models,. In: SAGE.

Langston, C. A. (1979). Structure under Mount Rainier, Washington, inferred from teleseismic body waves. *Journal of Geophysical Research: Solid Earth*, *84*(B9), 4749-4762. https://doi.org/https://doi.org/10.1029/JB084iB09p04749

Ligorría, J. P., & Ammon, C. J. (1999). Iterative deconvolution and receiver-function estimation. *Bulletin of the Seismological Society of America*, *89*(5), 1395-1400. https://doi.org/10.1785/bssa0890051395

Liu, M., & Gao, H. (2022). Three-Dimensional Variation of the Slab Geometry Within the South American Subduction System. *Geophysical Research Letters*, *49*(2), e2021GL095924. https://doi.org/https://doi.org/10.1029/2021GL095924

Michelini, A., Cianetti, S., Gaviano, S., Giunchi, C., Jozinović, D., & Lauciani, V. (2021). INSTANCE – the Italian seismic dataset for machine learning. *Earth Syst. Sci. Data*, *13*(12), 5509-5544. https://doi.org/10.5194/essd-13-5509-2021

Mousavi, S. M., Sheng, Y., Zhu, W., & Beroza, G. C. (2019). STanford EArthquake Dataset (STEAD): A Global Data Set of Seismic Signals for AI. *IEEE Access*, *7*, 179464-179476. https://doi.org/10.1109/ACCESS.2019.2947848

NCDEC. (2014). *Northern California Earthquake Data Center* (https://doi.org/10.7932/NCEDC

Rondenay, S. (2009). Upper Mantle Imaging with Array Recordings of Converted and Scattered Teleseismic Waves. *Surveys in Geophysics*, *30*(4), 377-405. https://doi.org/10.1007/s10712-009-9071-5

SCEDC. (2013). *Southern California Earthquake Center* (https://doi.org/10.7909/C3WD3xH1

Sheehan, A. F., Shearer, P. M., Gilbert, H. J., & Dueker, K. G. (2000). Seismic migration processing of P-SV converted phases for mantle discontinuity structure beneath the Snake River Plain, western United States. *Journal of Geophysical Research: Solid Earth*, *105*(B8), 19055-19065.

Thurber, C. (2015). *Laguna del Maule Seismic Imaging* (https://doi.org/10.7914/SN/ZR_2015

Zawacki, E. E., Bendick, R., & Woodward, R. L. (2023). Advancing Geophysics: IRIS and UNAVCO Merge to Form EarthScope Consortium. *Perspectives of Earth and Space Scientists*, *4*(1), e2023CN000227. https://doi.org/https://doi.org/10.1029/2023CN000227

Zhong, Y., & Tan, Y. J. (2024). Deep-Learning-Based Phase Picking for Volcano-Tectonic and Long-Period Earthquakes. *Geophysical Research Letters*, *51*. https://doi.org/10.1029/2024GL108438